International Journal of Heat and Mass Transfer 197 (2022) 123329

Contents lists available at ScienceDirect

International Journal of Heat and Mass Transfer

journal homepage: www.elsevier.com/locate/hmt

Enhanced boiling heat transfer by nucleation patterning with self-assembly of reduced graphene oxide coating

Geehong Choi[a,1], Maroosol Yun[b,1], Wei-Ting Hsu[b], Dong Il Shim[b], Donghwi Lee[c], Beom Seok Kim[d], Hyung Hee Cho[b,*]

[a] Hyundai Steel Co. Ltd., Chungcheongnam-do, Republic of Korea
[b] Department of Mechanical Engineering, Yonsei University, Seoul 03722, Republic of Korea
[c] Department of Mechanical System Engineering, Jeonbuk National University, Jeollabuk-do 54896, Republic of Korea
[d] Department of Mechanical and Automotive Engineering, Seoul National University of Science and Technology, Seoul 01811, Republic of Korea

ARTICLE INFO

Article history:
Received 15 June 2022
Revised 25 July 2022
Accepted 4 August 2022
Available online 11 August 2022

Keywords:
Nucleation patterning
Reduced graphene oxide
Self-assembly
Boiling heat transfer
Heat transfer coefficient

ABSTRACT

Boiling heat transfer is a favorable method for cooling high heat flux devices, and its performance is evaluated using critical heat flux (CHF), which indicates the maximum heat dissipation capacity. CHF occurs when a surface is covered with a vapor film due to bubble coalescence. Here, we propose a new nucleation patterning surface using rGO-coated micropillar-free cavities in order to enhance boiling heat transfer by suppressing bubble coalescence. Nucleation patterned surface is achieved by a sectored self-assembly on surfaces with artificial cavities embedded in micropillar array. The nucleation pattern is designed with spacings of 1.0 and 1.5 mm, with reference to the bubble departure diameter on the rGO-coated micropillar surface. The rGO particles deposited on the bottom of the micropillar-free cavity cause bubble formation in the cavities, and the micropillars around the cavities supply liquid to bubbles through wicking. Moreover, rGO deposition with varying heat flux schemes suggests the capability of constructing toned rGO layers on patterned micropillar surfaces. The results confirmed that high heat transfer performance can be obtained by applying denser bubble nucleation with a bubble generation spacing to bubble departure diameter ratio of 1, under the condition of preventing bubble coalescence. The heat transfer coefficient and critical heat flux were augmented by 340% and 203%, respectively, by preserving flow paths for water imbibition under the floating rGO layer and delaying bubble coalescence.

1. Introduction

Boiling is an efficient heat transfer method, and is applied to electronic equipment, heat exchanger tubes, nuclear power generation, and fusion power generation. In particular, boiling is attracting attention as a solution to the problem of cooling big data storage devices, which is becoming an important issue with the recent 4th Industrial Revolution [1]. Through boiling, low temperature of a heating surface can be maintained by changing the phase of the coolant. Performance factors of boiling are heat transfer coefficient (HTC), which indicates heat transfer efficiency, and critical heat flux (CHF), which indicates the maximum heat removal capacity to maintain stable surface temperature. If the surface heat flux exceeds CHF, a vapor film forms on the surface and blocks liquid supply. Consequently, the surface temperature suddenly rises, and surface damage occurs. The improvement of CHF is therefore important to protect heating surfaces from thermal failure.

To delay vapor film formation, bubble coalescence must be suppressed to maintain the liquid path to the surface. Bubble coalescence is the merging of adjacent bubbles to form larger bubble. In order to reduce bubble coalescence, research is actively being conducted to control bubble characteristics, for which surface treatment is an efficient approach. The nanowire structure reduces the critical wave length and induces active nucleate boiling [2]. Bubbles of small diameters depart at a faster frequency on the nanowire surface, resulting in improved heat transfer and higher CHF performance [3]. Nanoparticle coating with graphene/graphene-oxide nanofluid also improves the heat transfer performance by generating small bubbles in the porous structures which contain numerous micro-cavities [4,5]. The microstructure was designed such that the evaporation momentum acts in one direction to strengthen the bubble departure motion [6]. Thus, the micro/nanostructured surface could achieve improved heat transfer performance through active nucleate boiling. However, bubble

* Corresponding author.
E-mail address: hhcho@yonsei.ac.kr (H.H. Cho).
[1] These authors contributed equally to this work.

https://doi.org/10.1016/j.ijheatmasstransfer.2022.123329
0017-9310/

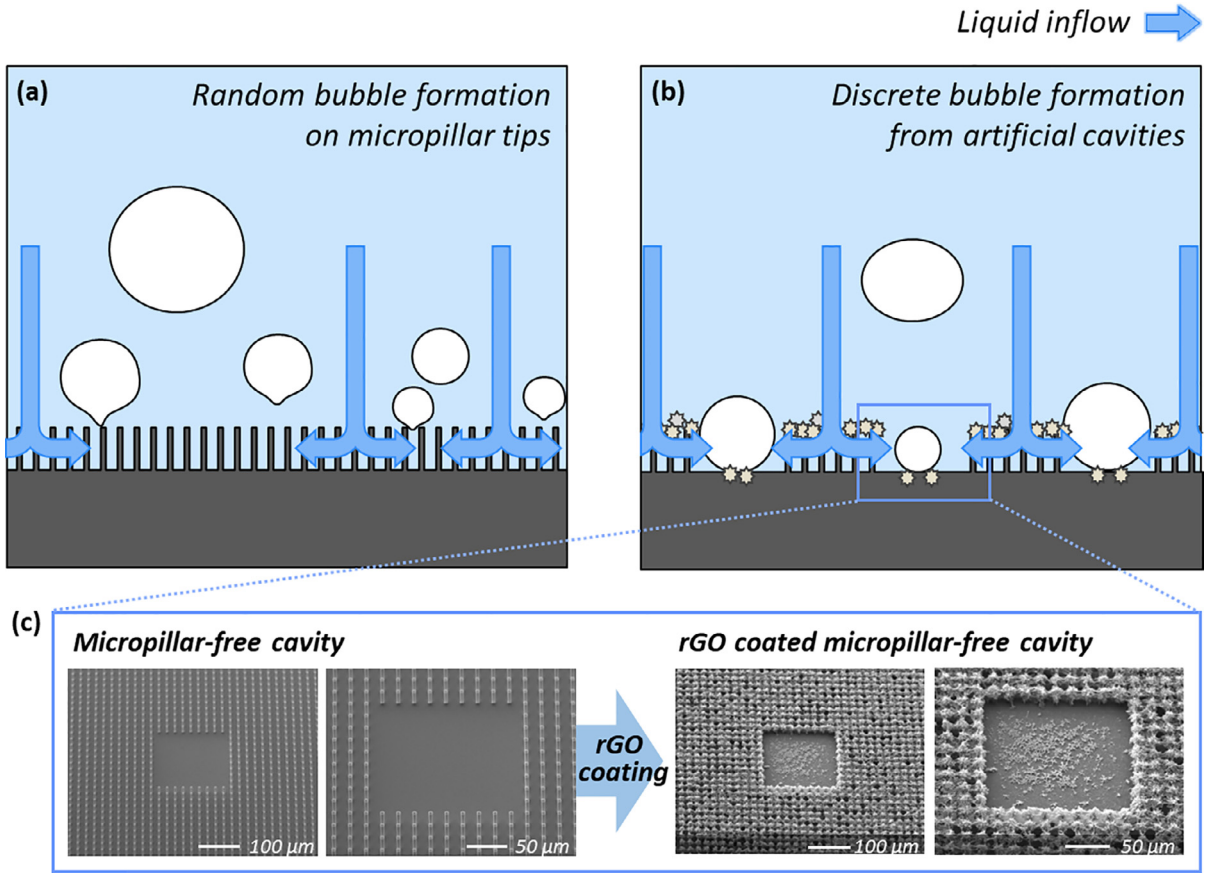

Fig. 1. Concept of nucleation patterning. (a) Random bubble formation on micropillar tips and liquid inflow in micropillar array, (b) artificial cavities determine discrete bubble formation sites with stable liquid paths through micropillar array, (c) preparation process of an actuated patterned surface with a bisected self-assembly.

coalescence that occurs under the condition of high heat flux is difficult to prevent.

To overcome this limitation, researchers attempted to reduce bubble coalescence by controlling the location of bubbles. Bi-conductive surfaces have been used to control the space between nucleated bubbles. Bi-conductive surfaces comprising materials with different thermal conductivities induce spatial variations in wall temperature. Bubbles are generated in the high temperature region and the low temperature region is utilized as the liquid flow path. In this manner, the liquid path can be stably maintained in the high heat flux region [7]. Studies have also been carried out to control the location of bubbles by constructing an artificial cavity structure. HTC increased with increasing cavity density, but CHF decreased in denser cavities because of the horizontal coalescence of bubbles [8]. Designing hydrophobic patterns on hydrophilic surfaces is another means of controlling bubble characteristics. Due to the difference in surface energy, the hydrophobic pattern acts as a bubble nucleation site [9,10]. Therefore, studies are underway to analyze the bubble behavior and heat transfer characteristics according to the optimum ratio of hydrophobic to hydrophilic area or the size and spacing of the hydrophobic pattern [11–13].

In general, efforts are continuously being made to improve the heat transfer by controlling the bubble departure characteristics through surface treatment using various methods of maintaining liquid paths by wicking phenomena or separating liquid-vapor pathway [14,15], controlling bubble nucleation with bi-conductive or biphilic surfaces to heighten CHF limits [7–13]. From these statics, we propose a new concept of nucleation patterning surface using rGO-coated micropillars (Fig. 1). The nucleation pattern was designed to reduce bubble coalescence, and bubble generation spacing was changed to secure a space for liquid supply between bubbles. By defining bubble nucleation sites, discrete and arranged bubble formation occurs since the predetermined cavities become active nucleation sites. This patterned surface morphology demonstrates a rich porous layer on the micropillar tips and only a thin layer on the cavity after nanofluid boiling. rGO particles deposited on the bottom of the cavity cause bubbles to form in the cavity, and the micropillars around the cavity supply the liquid through wicking. This different self-assembly behavior via nanofluid boiling can help to design engineering applications with controlled interfacial interactions. The bubble behavior and heat transfer characteristics were analyzed by changing the spacing of the nucleation pattern to 1.0 and 1.5 mm.

2. Materials and methods

2.1. Synthesis of reduced graphene oxide (rGO)

The reduced graphene oxide (rGO) was synthesized according to Hummer's method [16–18]. This method involves an oxidation reaction step and a reduction reaction step. Firstly, graphite, which has a two-dimensional graphene layer stacked by a van der Waals bond, is oxidized to graphite oxide. To oxidize graphite, graphite powder (1.5 g, 325 mesh, SP-1, Bay Carbon), $K_2S_2O_8$ (2.5 g, 99.99% purity, Sigma-Aldrich), and P_2O_5 (2.5 g, 99.99% purity, Sigma-Aldrich) are added to H_2SO_4 (12 mL, Duksan pure Chemicals). The solution is stirred at 120 °C for five hours, then cleaned and dried in the powder form. Then, the powder is put into H_2SO_4, and $KMnO_4$ (15 g, Junsei Chemical Co. Ltd) is added to the solution for five hours. The solution is kept at a temperature of 35 °C

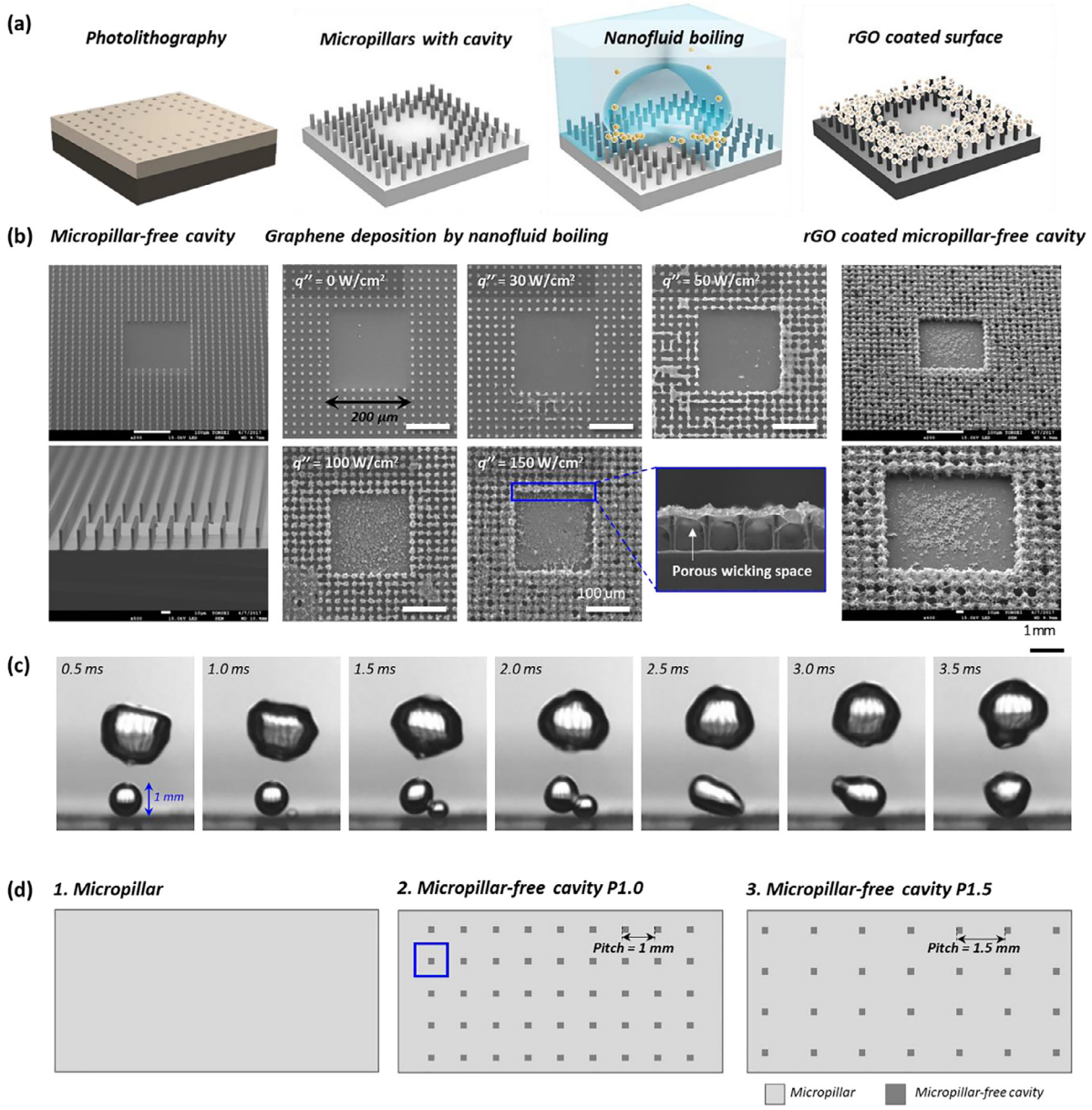

Fig. 2. Fabrication process and experimental cases. (a) Schematic diagram of Fabrication process. (b) SEM image of the rGO particle deposition process, (c) Single bubble departure diameter on rGO coated micropillar surface, (c) experimental cases of micropillar, P 1.0 and P 1.5.

and stirred overnight, after which it is diluted with 2.5 L water, and H_2O_2 (30 mL, Sigma-Aldrich) is added to the solution dropwise. The GO solution is washed with deionized (DI) water and HCl solution (1:10 of HCl and water, extra pure, Samchun Pure chemicals) to remove metal ions. Finally, the GO solution is reduced using Hydrazine monohydrate (3 μL) and ammonia solution (9 μL) at a temperature of 96 °C for two hours. For the boiling experiments, a concentration of 0.0005% of the rGO solution is used.

2.2. Patterned rGO coated surface

The design concept of the rGO-coated nucleation patterning surfaces could be better understood by describing the graphene structure fabrication process in Fig. 2. The nucleation patterning surface consists of a micropillar array and regularly arranged micropillar-free cavities. First, a positive photoresist (AZ GXR 601, 46CP) is coated on a silicon substrate and UV lithography is performed using a pattern mask. In the lithography mask, dots with sizes the same as the diameter of the pillars are distributed in the area where the micropillar is to be fabricated. The patterned photoresist acts as a protection layer in the deep reactive ion etching (DRIE) process, leaving a micropillar structure with a diameter of 4 μm, a pitch of 20 μm, and a height of 20 μm after the etching process. After the DRIE process, the organic matter remaining on the surface is removed through plasma ashing and piranha cleaning. On the other hand, the micropillar-free cavity region has no mask pattern because it must be etched without photoresist protection.

Next, the prepared micropillar surfaces are coated with rGO for active nucleate boiling. The nanofluid boiling method is used for rGO coating [19–21]. The experimental equipment for boiling is set using 0.0005 wt% rGO solution as the working fluid. The specimen to be coated with rGO particles is installed in the test section and the heat flux applied to the heater is increased by 3 W cm^{-2}. The coating time is maintained for 10 min at each heat flux step, and

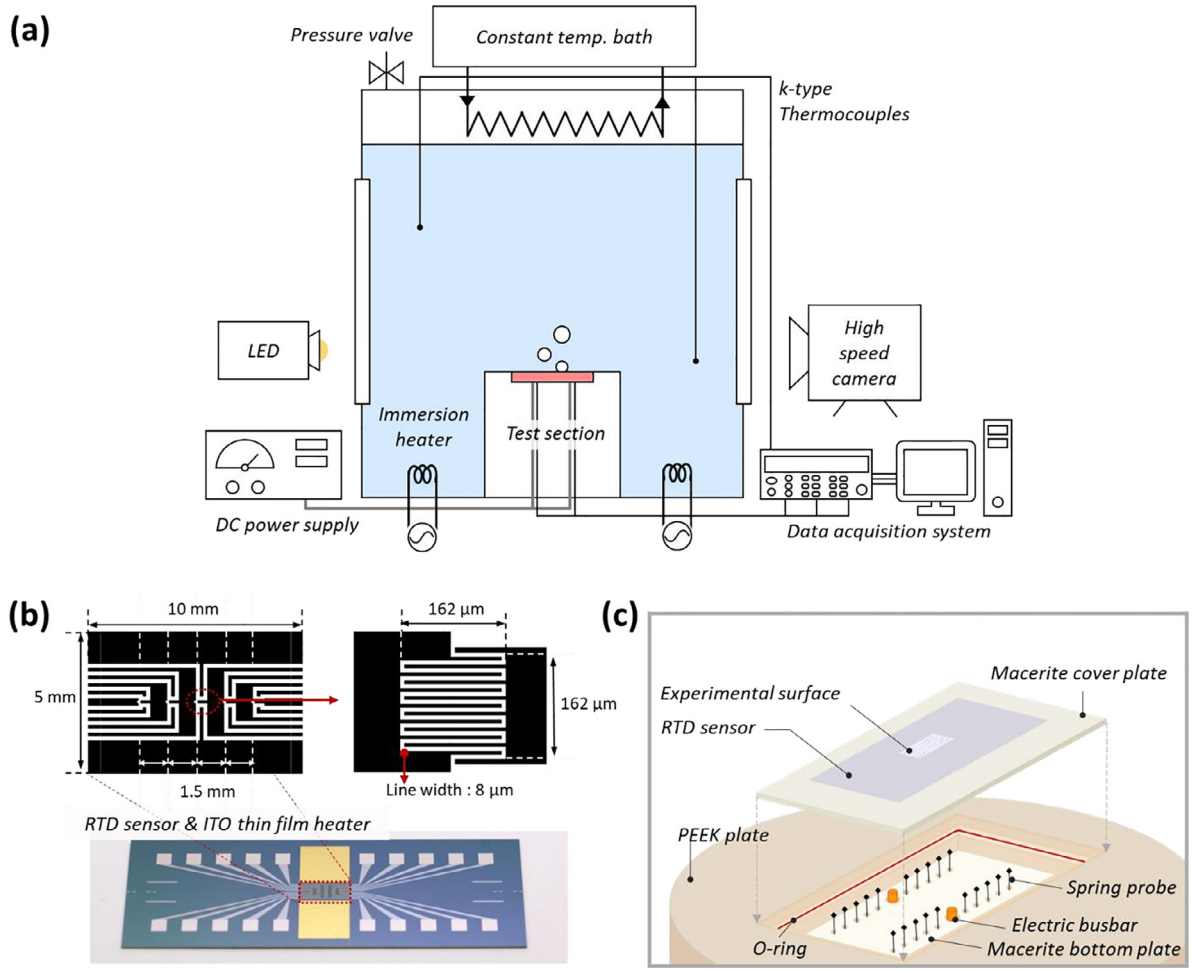

Fig. 3. Experimental system of the pool boiling heat transfer. (a) Experimental setup for pool boiling heat transfer, (b) Silicon chip with resistance temperature detector (RTD) sensors and indium tin oxide(ITO) thin film heater, (c) Test section assembly of the experimental setup.

the heat flux is increased until immediately before reaching CHF. The rGO coated specimens are evaluated for boiling heat transfer characteristics through boiling experiments using DI water as the working fluid.

The pitch of the nucleation pattern, (i.e. pitch of micropillar-free cavity) was designed based on the single bubble size of the rGO coated micropillar surface. Fig. 2c. indicates the bubble nucleation and bubble coalescence on the rGO coated micropillar surface. The size of the nucleating bubble is 1 mm. Since the purpose of this study aims to suppress bubble coalescence, bubble nucleation pitch was determined to be 1 and 1.5 mm to avoid the merger of the single bubble. Experimental cases are shown in Fig. 2d. Three types of microstructured surfaces were designed: in the first case, the overall surface was covered with micropillars; in the second case, micropillar-free cavities with an area of 200 μm $\times$ 200 μm were embedded into the micropillar array with a center-to-center pitch of 1 mm (P1.0, patterned surface); in the third case, micropillar-free cavities were arranged with a center-to-center pitch of 1.5 mm (P1.5, patterned surface). The pitch of the cavity was designed to evaluate the impact of the vacancy distance on the boiling nucleation and sequential coalescence of the bubbles [22,23].

2.3. Boiling heat transfer experiment

Fig. 3 shows the boiling heat transfer experimental system. The boiling experiments were performed at atmospheric pressure and saturated temperature of the working fluid, and DI water was used as the working fluid. The working fluid was introduced into the boiling chamber and its temperature was measured using two k-type thermocouples. Four auxiliary immersion heaters were installed in the chamber to raise and maintain the temperature of the working fluid. Prior to the experiment, gases dissolved in the working fluid were removed through a degassing process for 2 h. In the heat transfer experiment, a silicon chip was installed in the test section for the boiling test [24]. The silicon chip includes resistance temperature detector (RTD) sensors and indium tin oxide (ITO) thin film heaters, as shown in Fig. 3(b) The temperature-resistance correlation of the RTD sensor was obtained through pre-experiment temperature validation. Fig. 3(c) describes the test section assembly. RTD sensor after surface manipulation was put on the cover plate and assembled into the test section assembly. The test section surrounding the silicon chip sensor was made of low conductivity materials (PEEK (Poly Ethyl Ether Ketone), k_{PEEK} = 1.7 W/m•K and Macerite ceramic, $k_{Macerite}$ = 1.6 W/m•K) for thermal insulation. Macerite plates reduce heat spread and prevent sensor breakage due to abrupt temperature rise. Macerite plate put onto the PEEK plate to minimize heat spread in the test section. The thin film heater on the silicon chip was connected to a DC power supply (200 V–10 A, KSC Korea switching) with a couple of electric busbar and platinum pads on the sensor were connected to spring probes to collect data with a data acquisition system (34970A, Agilent Technologies, and SCXI-1503, National Instruments).

2.4. Data reduction

The heat flux (q'') is generated from the thin film heater and the value is calculated using the following equation

$$q'' = \frac{I \times V}{A} \tag{1}$$

where I is induced current, V is voltage, and A is heating area.

The wall temperature was measured using the RTD sensors, but the sensors were located on the backside of the heat transfer surface. Thus, the wall temperature is calculated according to Fourier's law for 1D thermal conduction as shown below:

$$T_w = T_R - \frac{t}{k_{Si}} \cdot q'' \tag{2}$$

where T_w, T_R, t, and k_{Si} are the wall temperature, temperature measured using RTD sensors, thickness of silicon substrate, and thermal conductivity of silicon, respectively. Lastly, the heat transfer coefficient is investigated according to Newton's law for thermal convection, expressed as:

$$h = q''/\left(T_w - T_f\right) \tag{3}$$

where h and T_f are the heat transfer coefficient and temperature of the working fluid. The uncertainty of data reduction was calculated following a previous study, heat loss in the test section was examined by numerical simulation using a commercial CFD program, ANSYS Fluent. The estimated value of the heat loss is 6.36%, and the uncertainties of heat flux, wall superheat, and heat transfer coefficient were 6.4%, 6.4%, and 9.2%, respectively [3,25].

2.5. Bubble characterization

Bubble visualization was conducted using the shadowgraph method. In order to visualize the bubble on the boiling surface, LED lighting (100 W) and a high speed camera (Speedsense M110, Dantec) were installed along a straight line. Images were recorded with a frequency of 2000 Hz on the rGO-coated micropillar and nucleation patterning surfaces (P 1.0 and P 1.5). Based on the recorded bubble images, bubble characteristics were analyzed using a software platform for scientific imaging (DynamicStudio, Dantec Dynamics, Denmark). The pitch of nucleation site was measured using a scale bar calculated during the calibration process for visualization, and the bubble departure diameter was evaluated using the particle characteristic analysis function in the software platform. The imaging software evaluated the bubble departure diameter as the diameter of the spherical particle having the same surface as the measured object. The uncertainty of bubble diameter measurement is ±0.1 mm.

3. Results and discussion

3.1. Deposition characteristics of rGO particles on the patterned surface

We devised the activated patterned surface with rGO coating for boiling actuation by deep reactive ion etching (DRIE) followed by rGO deposition via nanofluid boiling. High-aspect-ratio micropillar arrays were densely designed in advance to ensure sufficient capillary inflows for liquid replenishment over the surface [24].

To coat rGO layers on the structured surfaces, nanofluid boiling is performed using rGO particle solutions. When the bubble nucleation starts during nanofluid boiling, a microlayer is formed beneath the bubble, and evaporation occurs in the microlayer [19,26]. During the evaporation of the microlayer, rGO particles floating in the nanofluid do not escape into the bulk working fluid but settle on the solid surface by van der Waals force [19]. Since the deposition of the particles occurs at the microlayer, the location of the microlayer during nucleate boiling determines where rGO particles are formed. The spatial microlayer location varies with the nucleate boiling regime; thus, the deposition scheme of rGO particles can be changed as the heat flux increases.

Scanning electron microscopy (SEM) images in Fig. 4(a) show the characteristics of rGO layer deposition on patterned surfaces with different heat flux regimes during the nanofluid boiling process. Fig. 4(b) shows the schematic diagram of the particle deposition, bubble visualization, and rGO-coated surface under a partial nucleate boiling regime with a relatively low heat flux of 20 W cm^{-2}. A liquid–vapor–solid triple line is likely to form at the edge of the micropillar-free cavity area where the bubble nucleation initiates. During the separated nucleation of single bubbles, rGO particles are settled along with the edge of the microlayer, forming concentric coffee ring-like circles [27,28]. As this seed bubble grows, the bubble growth occurs with microlayer evaporation on micropillar tips so that rGO particles preferentially coat micropillars tips, which surround pillar-free cavities. As a result, rGO coating starts to form at the bottom of the artificial cavity and then expands onto the tips of the micropillar array, as illustrated in Fig. 4(b). When the heat flux increases to 50 W cm^{-2} to a fully developed boiling regime, the bubble hovers above the micropillar structures and microlayer is formed as water menisci between the pillar due to the stable wicking [24]. Therefore, newly depositing particles interconnect the tips, and this leads to a rich, floating layer of rGO on the micropillars, as shown in Fig. 4(c).

For higher heat fluxes above 150 W cm^{-2}, which could trigger surface dry-out, the shape of the microlayer for this high heat flux develops into the small liquid reservoir at the corners of the microstructure [29]. Thus, the triple line goes to the edge of the porous layer and down to the lateral sides of the micropillar. As presented in Fig. 4(d), rGO particles thicken the rGO coating and cover even the root and side surfaces of the micropillar. For the rGO layer on the pillar-free cavity side, it stays quite thin even for high heat fluxes, as shown in Fig. 4(a). These stepwise experimental approaches imply that the conformation of rGO particle deposition can be manipulated exquisitely by controlling the applied heat fluxes during nanofluid boiling. Further, the deposition of rGO particles could be tailored by tuning the deposition time under the corresponding heat flux.

3.2. Boiling performances of the nucleation patterned surface

The impact of the rGO deposition for activated patterned surfaces on the cooling performance of two-phase heat dissipation is annotated after surface preparation. For boiling experiments with the rGO-coated surfaces, heat flux is gradually increased from the onset of bubble nucleation and until immediately before the specimens' CHF point to enrich the porous rGO layer. Bubble generation characteristics can be distinguished by bubble visualization according to both the surface condition and the heat flux, as indicated in Fig. 5. At the initial stage of boiling, bubbles are randomly generated on the rGO-coated micropillar surface, and adjacent bubbles merge, while bubbles on the activated patterned surfaces (P1.0 and P1.5) initiate from the artificial cavities. As shown in Fig. 5(a), the ripples on the bubble surface at a heat flux of 10 W cm^{-2} indicate that bubble coalescence has occurred, and following capillary waves affect the shape of a rising bubble. As the heat flux increases, the coalescence of bubbles becomes more vigorous, causing them to float in the form of columns. Moreover, activated patterned surfaces enable the dispersal of bubble nucleation for both lower and higher heat fluxes, as shown in Fig. 5(b) and (c). At a heat flux of 10 W cm^{-2}, the bubble interface seems to be spherical without any ripples as nucleation sites are confined to the

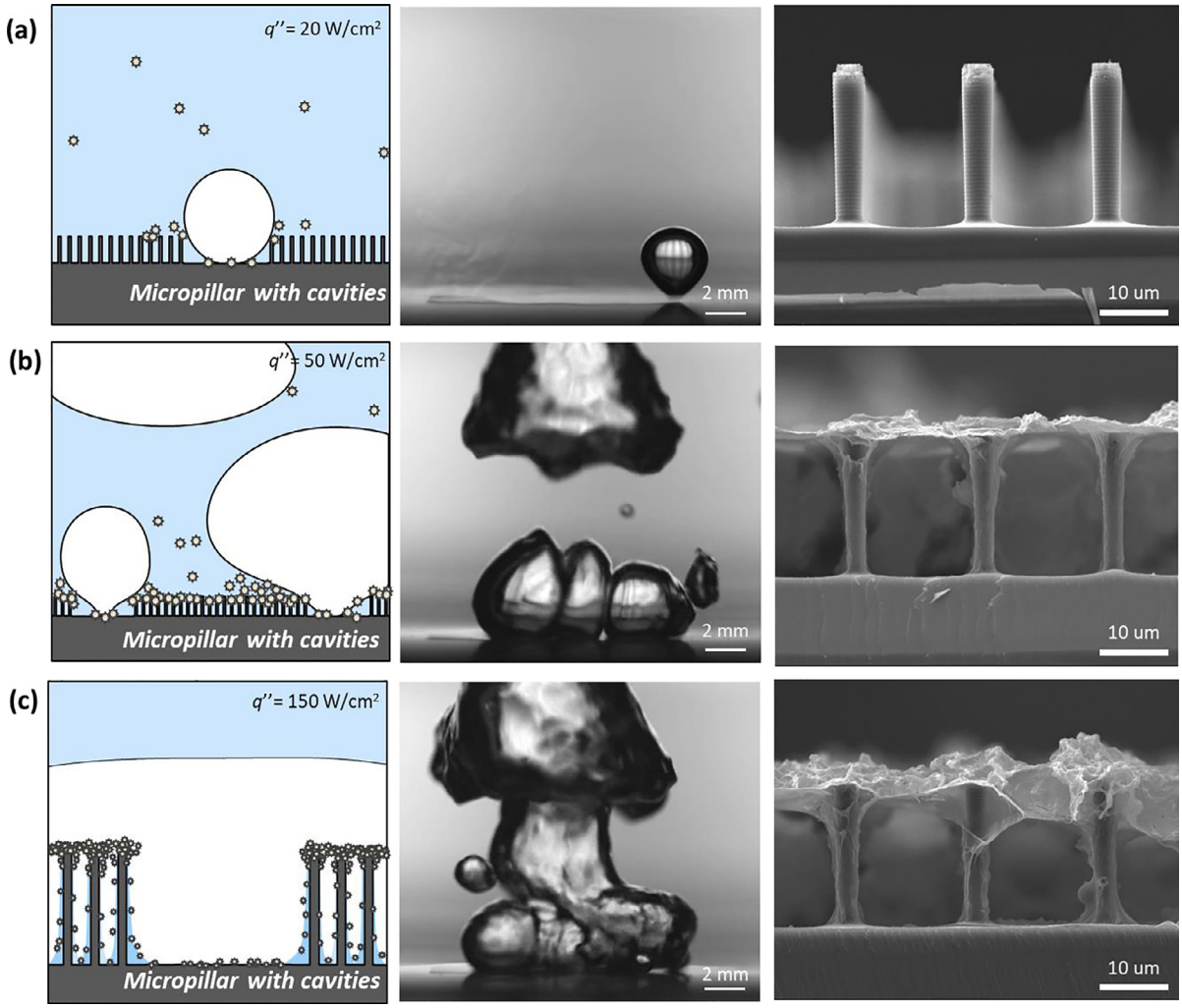

Fig. 4. Schematic diagram on formation of porous rGO layer on the nucleation patterning surfaces, the liquid–vapor–solid triple line, bubble visualization during the rGO deposition process, SEM images of the resulting surfaces (a) for partial nucleate boiling with low heat fluxes, (b) for matured nucleate boiling with medium heat fluxes, (c) before the transition to film boiling with high heat fluxes.

pre-patterned cavities with a thin rGO layer, and individual bubble shape keeps intact without coalescence. The morphological impact of the activated patterned surfaces is confirmed at a heat flux of 50 W cm^{-2}, where the intended pitches between the cavities play a critical role in hindering bubble coalescence. Minor coalescence of departing bubbles is monitored on P1.0 and P1.5 surfaces, and the shape of individual bubble stems is maintained.

Passages between bubbles, which are occupied with liquid and ensure better liquid accessibility, are distinguishable on both surfaces (*i.e.*, P1.0 and P1.5), as marked by spacings between yellow arrows in Fig. 5(b) and (c). An increase in the number of these spaces can be observed on the P1.5 surface compared with that on the P1.0 surface, which is advantageous. When designing the cavity pattern, we set the pitch between the cavities based on a bubble size of 1 mm on the rGO-coated micropillar surface (Fig. 2(c)). However, the size of the departing bubbles on the activated patterned surfaces increased slightly compared to those of the rGO-coated micropillar surface as shown in the Fig. 5.

For the rGO-coated micropillar surface, heat is dispersed in adjacent cavities in the porous rGO layer. Thus, the bubbles cannot grow sufficiently due to the dispersed heat. However, on the P1.0 and P1.5 surfaces, bubbles are generated in the pillar-free cavity owing to sufficient spacing. Therefore, the localized heat is transferred to each cavity on the patterned surfaces, resulting in a slight increase in the sizes of the bubbles, as depicted in the insets in Fig. 5. Larger bubbles are generated on the P1.0 surface compared with those generated in the designed cavity pitch; therefore, bubble coalescence occurs more easily. Bubble coalescence interrupts the liquid supply and narrows the liquid supply path. However, cavities in the P1.5 surface functions independently without early bubble coalescence at a heat flux of 50 W cm^{-2}. Therefore, Fig. 5(c) shows more liquid paths are secured in P1.5 than in P1.0, indicating that rGO nucleation patterning is activated efficiently.

When bubbles depart with less coalescence, the time occluded by the bubble film is relatively short, and the surface temperature is kept low without significant overheating as the liquid inflow is ensured. The amount of heat removed per unit area is increased by these passages between bubbles. Fig. 6 shows the HTC results during boiling heat transfer on a plain surface, micropillars, and P1.0 and P1.5 surfaces with rGO coating. As nucleate boiling develops with the increased heat flux, the HTC gradually increases, regardless of the interface conditions. Nevertheless, the maximum HTC depends on the nucleation characteristics on each surface, which are directly related to the two-phase convection. After rGO coating, the maximum HTC is improved by 96%, 96%, 108%, and 114% on the plain, P1.5, P1.0, and micropillar surfaces, respectively. Herein, P1.0 and P1.5, which are the rGO-coated surfaces with pillar-free cavities, show the utmost HTCs of 85.8 kW m^{-2} K^{-1}

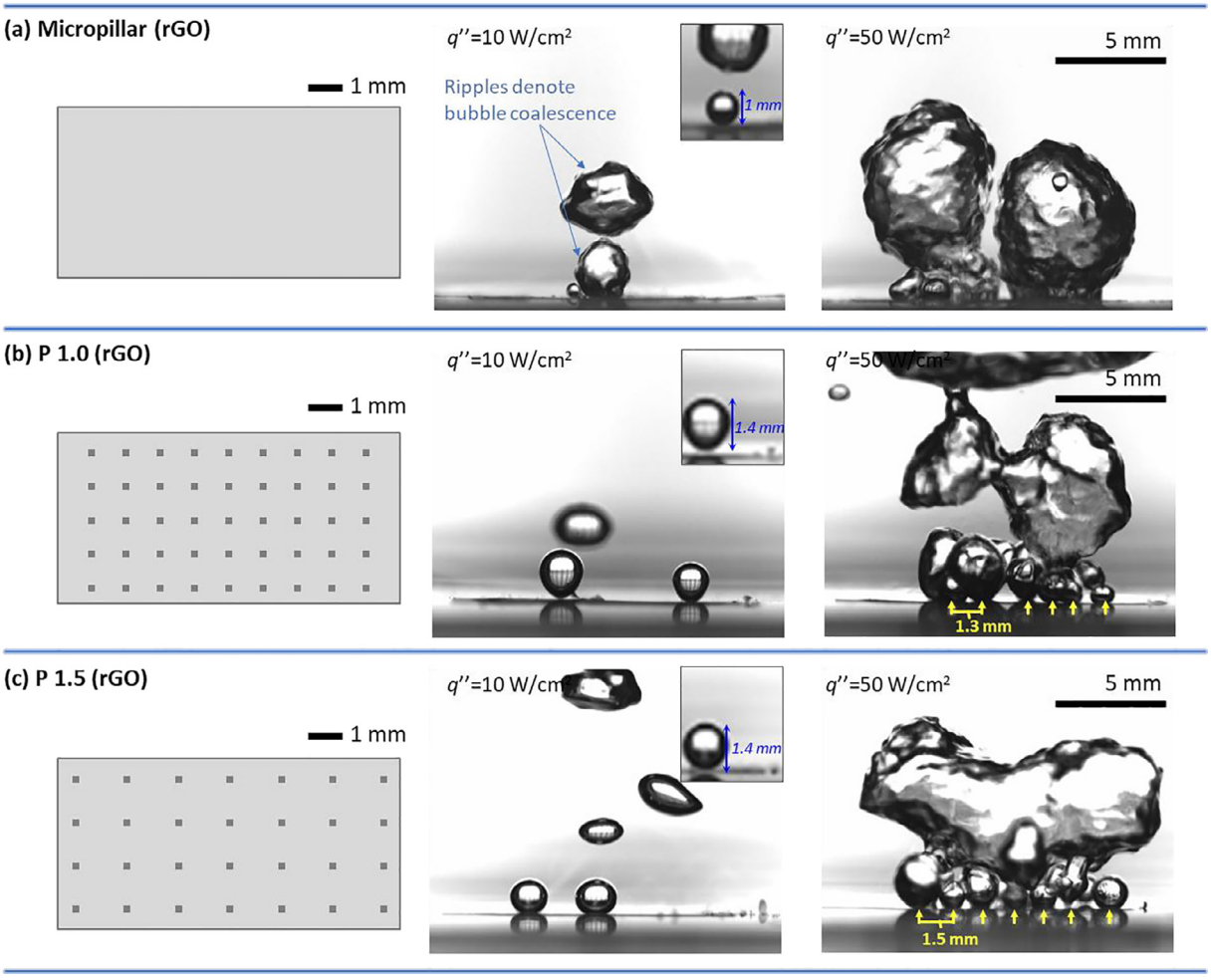

Fig. 5. Bubble departure characteristics on the nucleation patterning surface. Bubble visualization of (a) The micropillar array surface, (b) Surface with micropillar cavities arranged at 1 mm spacing (P1.0), and (c) Surface with micropillar cavities arranged at 1.5 mm spacing (P1.5). Insets in the second column of the figure indicate the single bubble diameter at the onset of bubble nucleation of each surface. The yellow arrows mark the location of bubble nucleation. Scale bars on the surface description and bubble visualization image indicate 1 mm and 5 mm, respectively.

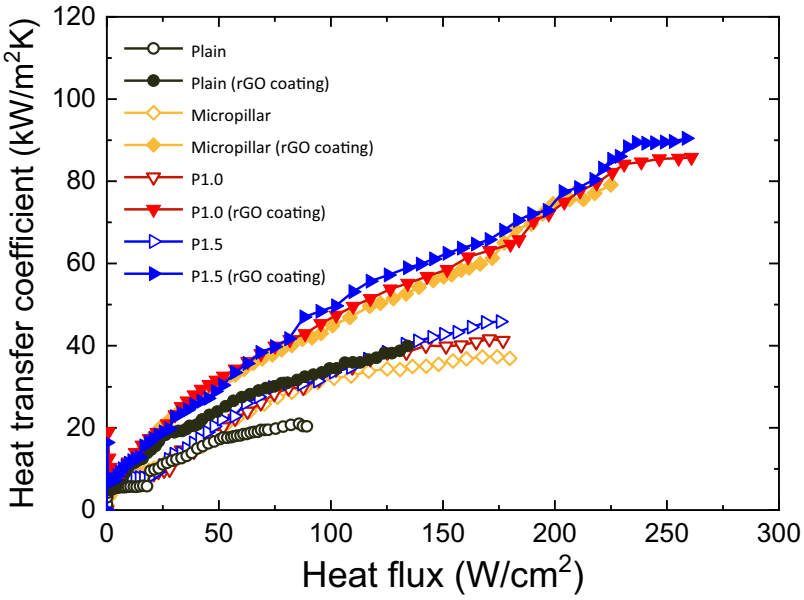

Fig. 6. Distributions of HTC on the plain surface, micropillar surface, P 1.0 surface, and P 1.5 surface with and without rGO coating.

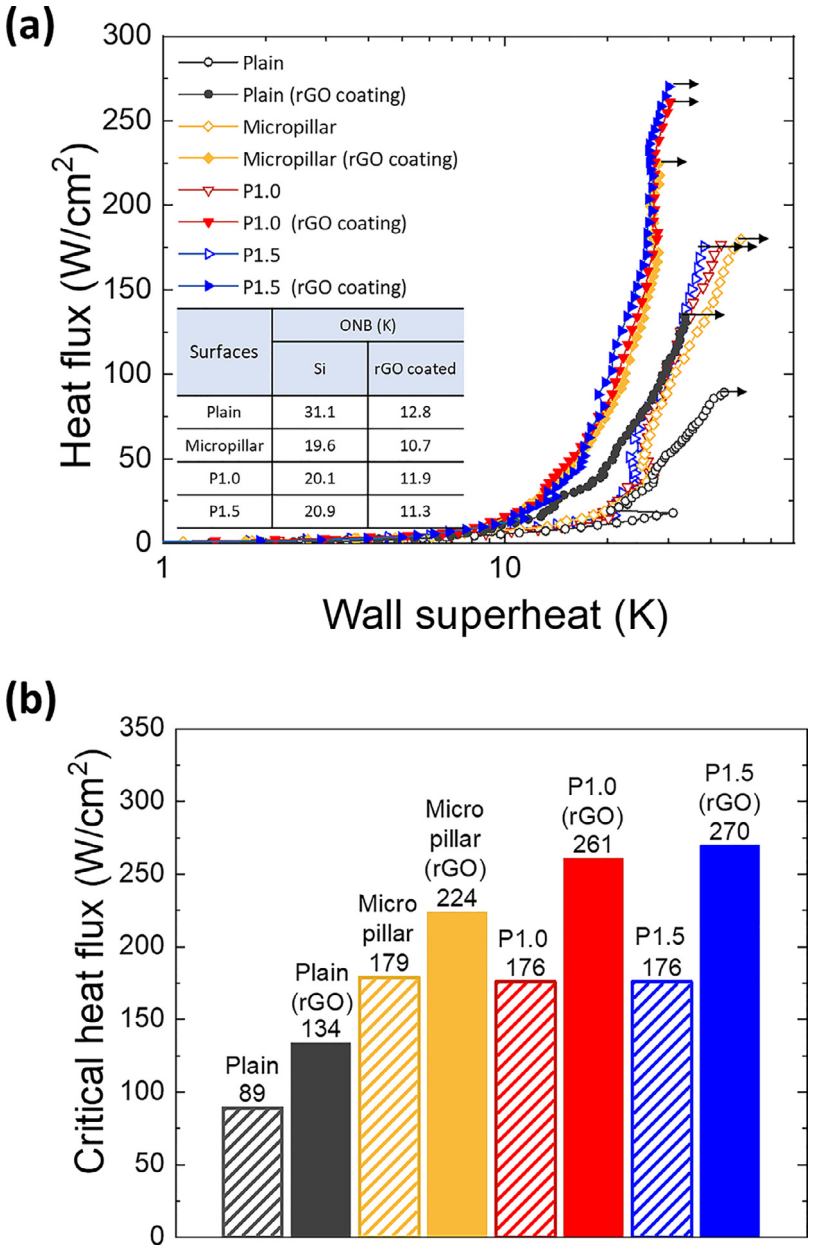

Fig. 7. Impact of the bisected self-assembly on boiling performances of CHF and ONB on a plain, micropillars, P1.0, and P1.5 surface. (a) Boiling characteristic curves, and (b) comparison of CHFs according to the rGO coating.

and 89.7 kW m^{-2} K^{-1}, respectively, whereas it is 79.1 kW m^{-2} K^{-1} for the rGO-coated micropillar surface. As previously discussed in the bubble visualization results based on surface manipulations, the dispersed bubbles on the activated patterned surface efficiently dissipate heat through separated and dispersed ebullition so that the HTC can be further improved beyond the rGO-coated surface without beneficial microcavities.

If bubbles merge and form a vapor blanket covering the heated surface, the vapor blanket blocks the liquid replenishment and finally causes surface failure due to an abrupt increase in the wall temperature. Meanwhile, it is known that liquid passages between bubbles lead to stable and plenty of coolant supply toward the heated surface under the boiling heat transfer [26,29,30]. In particular, the aforementioned bubble behavior and the accompanying potential for the liquid supply on the rGO-coated surface improve the CHF. Fig. 7 shows boiling curves and CHF distributions on plain, micropillar, and P1.0 and P1.5 surfaces with and without rGO coating. In Fig. 7(a), the boiling curve of the plain surface with rGO coating moves to the left than that of the plain surface without coating. This explains that the wall superheat on the rGO-coated surface is reduced under the equivalent heat flux condition. The wall superheat reduction is also evident on the micropillar surface. This lower wall superheat in the presence of rGO coating could be explained by the high thermal conductivity and the nucleation-promoting effect of rGO. The thin rGO layer on the microcavities of P1.0 and P1.5 surfaces has smaller cavities with an effective diameter of a couple of microns, which are suitable for bubble nucleation [19]. The phase change due to active bubble generation and the following turbulent convection along the upward bubbly flow can effectively dissipate more heat per unit area to the working fluid. Furthermore, the high thermal conductivity of rGO benefits the growth of the bubble nucleus, initiating nucleate boiling with low thermal energy. The onset of nucleate boiling (ONB) is encouraged for lower wall superheat on the rGO-coated surface. The inset

Table 1
Comparison results of averaged nucleation pitch, bubble diameter, and normalized pitch of bubbles on experimental surfaces and Ref. [22].

	Averaged pitch (mm)	Averaged diameter (mm)	P_{avg}/D_{avg}
P 1.0	1.0	7.6	0.13
P 1.5	1.5	8.1	0.18
rGO-coated micropillar	0.8	1.0	0.79
rGO-coated P 1.0	1.0	1.2	0.83
rGO-coated P 1.5	1.5	1.4	1.04
Plain [22]	3.6	3.0	1.20
Microcavity [22]	1.0	2.5	0.42
Nanowires [22]	0.7	1.1	0.60
MNHS [22]	1.0	1.0	1.00

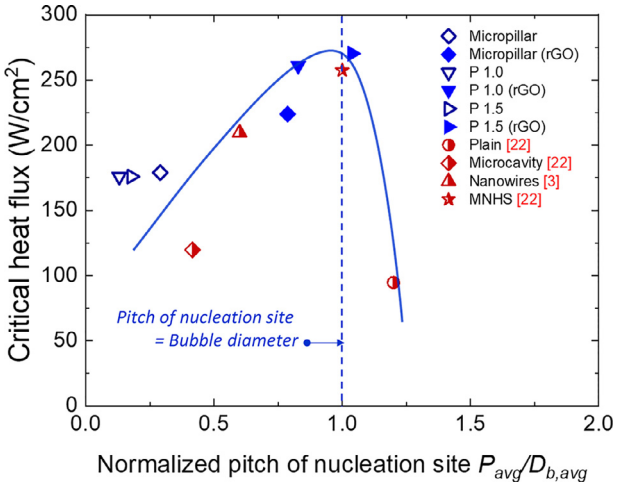

Fig. 8. Distribution of CHF under the activated nucleation pattern effect according to the normalized pitch of nucleation site. The dotted line represented that the ratio of pitch of nucleation site over the bubble departure diameter is 1.

table in Fig. 7(a) shows the ONB temperature of each surface. After the rGO self-assembly, the ONB point of surfaces with micropillar is reduced to 10 K.

Fig. 7(b) shows the impact of rGO coating on the CHF enhancement of the plain, micropillar, and activated patterned surfaces. The surfaces with micropillars inherently exhibit higher CHF than the plain surface owing to wicking between bubbles. Moreover, CHF is significantly improved on the rGO-coated surfaces. In particular, remarkable CHF values of 261 W cm^{-2} and 270 W cm^{-2} are obtained from P1.0 and P1.5 activated patterned surfaces, respectively. Pattern surfaces without rGO coatings show similar CHF values as micropillar surfaces, but after rGO deposition, the designed micropillar-free cavity is activated by the bisected self-assembly, which leads to improved heat transfer. The bisected self-assembly on the patterned surfaces extends nucleate boiling to a higher heat flux by controlling the location of bubble formation and securing liquid paths between bubbles. The securing of the liquid supply path retards bubble coalescence and suppresses vapor film formation. As a result, the highest CHF is obtained from the P1.5 surface, where the liquid supply passage between the bubbles is secured, as illustrated in the bubble visualization. The CHF of the P1.5 surface shows a 3-fold enhancement compared to that of the plain surface.

The CHF increase can be demonstrated by a function of the normalized pitch of the nucleation site ($P_{avg}/D_{b,avg}$) on activated patterned surfaces, as shown in Fig. 8. P_{avg} indicates the pitch of the bubble nucleation site, and $D_{b,avg}$ means the averaged diameter of single bubbles. Detailed dimensions of the bubble size and pitch are shown in Table 1. The red symbols represent data reported in our previous study [22]. Since the plain surface has not only a larger bubble nucleation pitch than the bubble size ($P_{avg}/D_{b,avg} > 1$) but also a small bubble nucleation density due to the lack of any artificial cavities, the plain surface has a low CHF due to its small heat dissipation capacity. The micropillar surfaces have a higher CHF than the plain surface owing to capillary inflow, which induces vapor film formation. However, it generates bubbles larger than 7 mm ($P_{avg}/D_{b,avg} < 1$), which interferes with the liquid supply to the heating surface, limiting the heat transfer improvement by suppressing the capillary inflow. For the rGO-coated micropillar surface, nucleation site density could be increased as rGO deposition leads to a dense bubble generation, which induces enhanced heat dissipation capacity. Specifically, small-diameter bubbles ($D_{b,avg} = \sim 1$ mm) are generated from the porous rGO structures, whereas those bubbles have an average pitch of approximately ~0.75 mm among bubbles so that bubble coalescence can be suppressed in this regime ($P_{avg}/D_{b,avg} < 1$). The activated patterned surfaces can disperse bubble nucleation spots and shift the normalized pitch for nucleation sites to 1. This means that the most efficient heat transfer performance could be achieved by maximizing the nucleation site density and suppressing bubble coalescence, thereby securing the liquid path on activated patterned surfaces, verifying that the nucleation patterning on the heated surface could act as an effective CHF improvement methods compared to the other CHF improvement methods of surface roughening, structure inducing capillary wicking, or saving liquid paths without maximizing the nucleation density. Consequently, a normalized pitch of nucleation sites could be a principal design factor for determining heat transfer performance through controlling bubble characteristics. This approach can guide the design of thermal management interfaces for computer chip cooling, nuclear reactors, and HCPV cell, which need reliable heat dissipation on a hot spot.

4. Conclusion

In this study, we propose a new concept of nucleation patterning of surface using an rGO-coated micropillar-free cavity with the patterned self-assembly of rGO, enabling an engineered interfacial interaction. In particular, the rGO-coated micropillar-free cavity facilitated bubble nucleation by providing a suitable sized cavity in the porous rGO structure and the location of nucleated bubbles can be controlled. The porous rGO layer formation is modified by the heat flux used during nanofluid boiling, and particle deposition could be tailored by heat flux control during the nanofluid boiling process. The spacing between the cavities was designed on the basis of the diameter of departing bubbles and this spacing could ensure liquid supply to the surface by securing the liquid path between bubbles. The liquid supply was ensured by preferentially coating the rGO layer on top of the pillars, allowing capillary inflow between the micropillar array. As a result, bubble coalescence was reduced, and vapor film formation was prevented. Moreover, the heat transfer coefficient and critical heat flux increased by 340% and 203%, respectively, on the nucle-

ation patterning surface compared to the plain surface. Through this study, it was confirmed that high heat transfer performance can be achieved by implementing the densest bubble nucleation with a bubble generation spacing to bubble departure diameter ratio of 1 under the condition of preventing bubble coalescence. We suggest that particle deposition by nanofluid boiling can be used for developing tailored interfaces and normalized pitch between nucleation spots can be optimized for improving the thermal design of phase-changing heat transfer in the future.

Declaration of Competing Interest

The authors declare no conflict of interest.

CRediT authorship contribution statement

Geehong Choi: Writing – original draft, Methodology, Formal analysis. **Maroosol Yun:** Writing – original draft, Methodology, Formal analysis. **Wei-Ting Hsu:** Formal analysis. **Dong Il Shim:** Formal analysis. **Donghwi Lee:** Writing – review & editing. **Beom Seok Kim:** Writing – review & editing. **Hyung Hee Cho:** Supervision, Writing – review & editing.

Acknowledgments

This work was supported by the Human Resources Development Program (No. 20204030200110) of the Korea Institute of Energy Technology Evaluation and Planning (KETEP) grant funded by the Korea government Ministry of Trade, Industry and Energy.

References

[1] C. Nadjahi, H. Louahlia, S. Lemasson, A review of thermal management and innovative cooling strategies for data center, Sustain. Comput. Inform. Syst. 19 (2018) 14–28.
[2] R. Chen, M.C. Lu, V. Srinivasan, Z. Wang, H.H. Cho, A. Majumdar, Nanowires for enhanced boiling heat transfer, Nano Lett. 9 (2) (2009) 548–553.
[3] B.S. Kim, S. Shin, D. Lee, G. Choi, H. Lee, K.M. Kim, H.H. Cho, Stable and uniform heat dissipation by nucleate-catalytic nanowires for boiling heat transfer, Int. J. Heat Mass Transf. 70 (2014) 23–32.
[4] H. Kim, J. Kim, M.H. Kim, Effect of nanoparticles on CHF enhancement in pool boiling of nano-fluids, Int. J. Heat Mass Transf. 49 (25-26) (2006) 5070–5074.
[5] S.M. Kwark, G. Moreno, R. Kumar, H. Moon, S.M. You, Nanocoating characterization in pool boiling heat transfer of pure water, Int. J. Heat Mass Transf. 53 (21-22) (2010) 4579–4587.
[6] S.G. Kandlikar, Controlling bubble motion over heated surface through evaporation momentum force to enhance pool boiling heat transfer, Appl. Phys. Lett. 102 (5) (2013) 051611.
[7] M. Shojaeian, A. Koşar, Pool boiling and flow boiling on micro-and nanostructured surfaces, Exp. Therm. Fluid Sci. 63 (2015) 45–73.
[8] M.M. Rahman, J. Pollack, M. McCarthy, Increasing boiling heat transfer using low conductivity materials, Sci. Rep. 5 (1) (2015) 1–11.
[9] A.R. Betz, J. Jenkins, D. Attinger, Boiling heat transfer on superhydrophilic, superhydrophobic, and superbiphilic surfaces, Int. J. Heat Mass Transf. 57 (2) (2013) 733–741.
[10] M.M. Rahman, M. McCarthy, Boiling enhancement on nanostructured surfaces with engineered variations in wettability and thermal conductivity, Heat Transf. Eng. 38 (14-15) (2017) 1285–1295.
[11] A.R. Motezakker, A.K. Sadaghiani, S. Celik, T. Larsen, L.G. Villanueva, A. Koşar, Optimum ratio of hydrophobic to hydrophilic areas of biphilic surfaces in thermal fluid systems involving boiling, Int. J. Heat Mass Transf. 135 (2019) 164–174.
[12] D.Y. Lim, I.C. Bang, Controlled bubble departure diameter on biphilic surfaces for enhanced pool boiling heat transfer performance, Int. J. Heat Mass Transf. 150 (2020) 119360.
[13] M. Može, M. Zupančič, I. Golobič, Pattern geometry optimization on superbiphilic aluminum surfaces for enhanced pool boiling heat transfer, Int. J. Heat Mass Transf. 161 (2020) 120265.
[14] A. Jaikumar, S.G. Kandlikar, Ultra-high pool boiling performance and effect of channel width with selectively coated open microchannels, Int. J. Heat Mass Transf. 95 (2016) 795–805.
[15] S.G. Kandlikar, Enhanced macroconvection mechanism with separate liquid—vapor pathways to improve pool boiling performance, J. Heat Transf. 139 (5) (2017) 051501.
[16] J. Chen, B. Yao, C. Li, G. Shi, An improved Hummers method for eco-friendly synthesis of graphene oxide, Carbon 64 (2013) 225–229.
[17] S.N. Alam, N. Sharma, L. Kumar, Synthesis of graphene oxide (GO) by modified hummers method and its thermal reduction to obtain reduced graphene oxide (rGO), Graphene 6 (1) (2017) 1–18.
[18] N. Cao, Y. Zhang, Study of reduced graphene oxide preparation by Hummers' method and related characterization, J. Nanomater. 2015 (2015) 2–6, doi:10.1155/2015/168125.
[19] S.M. Kwark, R. Kumar, G. Moreno, J. Yoo, S.M. You, Pool boiling characteristics of low concentration nanofluids, Int. J. Heat Mass Transf. 53 (5-6) (2010) 972–981.
[20] H.S. Ahn, J.M. Kim, C. Park, J.W. Jang, J.S. Lee, H. Kim, M.H. Kim, A novel role of three dimensional graphene foam to prevent heater failure during boiling, Sci. Rep. 3 (1) (2013) 1–7.
[21] A. Jaikumar, S.G. Kandlikar, A. Gupta, Pool boiling enhancement through graphene and graphene oxide coatings, Heat Transf. Eng. 38 (14-15) (2017) 1274–1284.
[22] D. Lee, N. Lee, D.I. Shim, B.S. Kim, H.H. Cho, Enhancing thermal stability and uniformity in boiling heat transfer using micro-nano hybrid surfaces (MNHS), Appl. Therm. Eng. 130 (2018) 710–721.
[23] Singh, A., Mikic, B.B., & Rohsenow, W.M. Effect of superheat and cavity size on frequency of bubble departure in boiling. (1977). 246-249. doi:10.1115/1.3450676.
[24] G. Choi, D.I. Shim, D. Lee, B.S. Kim, H.H. Cho, Enhanced nucleate boiling using a reduced graphene oxide-coated micropillar, Int. Commun. Heat Mass Transf. 109 (2019) 104331.
[25] R.J. Moffat, Describing the uncertainties in experimental results, Exp. Therm. Fluid Sci. 1 (1) (1988) 3–17.
[26] M.G. Cooper, A.J.P. Lloyd, The microlayer in nucleate pool boiling, Int. J. Heat Mass Transf. 12 (8) (1969) 895–913.
[27] D.S. Eom, J. Chang, Y.W. Song, J.A. Lim, J.T. Han, H. Kim, K. Cho, Coffee-ring structure from dried graphene derivative solutions: a facile one-step fabrication route for all graphene-based transistors, J. Phys. Chem. C 118 (46) (2014) 27081–27090.
[28] S.H. Kang, Y.C. Shin, E.Y. Hwang, J.H. Lee, C.S. Kim, Z. Lin, S.W. Hong, Engineered "coffee-rings" of reduced graphene oxide as ultrathin contact guidance to enable patterning of living cells, Mater. Horiz. 6 (5) (2019) 1066–1079.
[29] J. Li, G. Zhu, D. Kang, W. Fu, Y. Zhao, N. Miljkovic, Endoscopic visualization of contact line dynamics during pool boiling on capillary-activated copper microchannels, Adv. Funct. Mater. 31 (4) (2021) 2006249.
[30] B.S. Kim, H. Lee, S. Shin, G. Choi, H.H. Cho, Interfacial wicking dynamics and its impact on critical heat flux of boiling heat transfer, Appl. Phys. Lett. 105 (19) (2014) 191601.